Physics in Medicine & Biology

IPEM Institute of Physics and Engineering in Medicine

Algebraic Helmholtz inversion in planar magnetic resonance elastography

To cite this article: S Papazoglou *et al* 2008 *Phys. Med. Biol.* **53** 3147

View the article online for updates and enhancements.

Related content

- Multifrequency inversion in magnetic resonance elastography
  Sebastian Papazoglou, Sebastian Hirsch, Jürgen Braun et al.
- Viscoelastic properties of soft gels
  R J Okamoto, E H Clayton and P V Bayly
- Ultrasound-based TE compared to MRE
  Jennifer Oudry, Jonathan Vappou, Philippe Choquet et al.

Recent citations

- Magnetic Resonance Elastography of Rodent Brain
  Mathilde Bigot *et al*
- Mapping the Viscoelastic Behavior of Soft Solids From Time Harmonic Motion
  Yue Mei and Sevan Goenezen
- Fast tomoelastography of the mouse brain by multifrequency single-shot MR elastography
  Gergely Bertalan *et al*

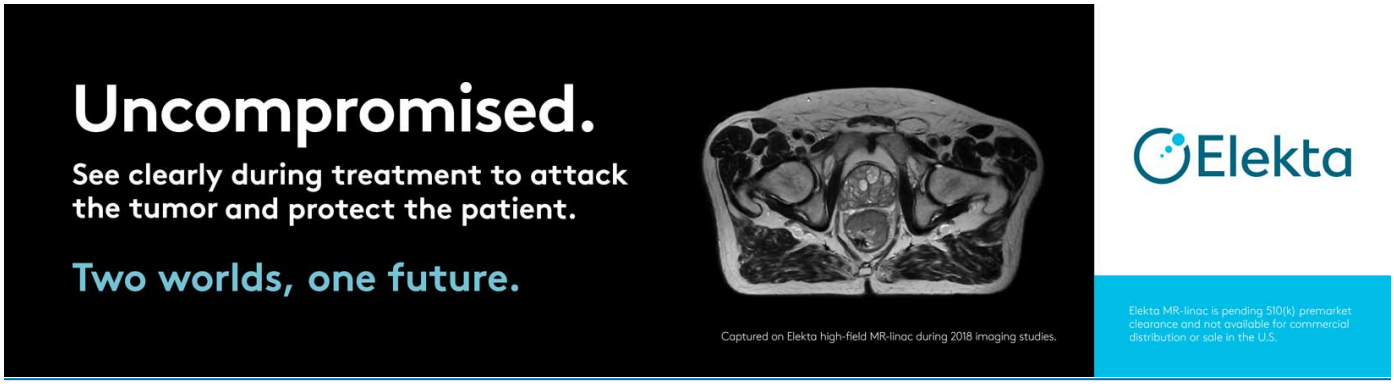

This content was downloaded from IP address 128.104.2.128 on 28/03/2019 at 03:06

IOP PUBLISHING PHYSICS IN MEDICINE AND BIOLOGY

Phys. Med. Biol. **53** (2008) 3147–3158 doi:10.1088/0031-9155/53/12/005

Algebraic Helmholtz inversion in planar magnetic resonance elastography

S Papazoglou[1], U Hamhaber[2], J Braun[2] and I Sack[1]

[1] Department of Radiology, Charite-Universitätsmedizin, Berlin, Germany
[2] Institute of Medical Informatics, Charite-Universitätsmedizin, Berlin, Germany

E-mail: ingolf.sack@charite.de

Received 19 February 2008, in final form 26 April 2008
Published 21 May 2008
Online at stacks.iop.org/PMB/53/3147

Abstract

Magnetic resonance elastography (MRE) is an increasingly used noninvasive modality for diagnosing diseases using the response of soft tissue to harmonic shear waves. We present a study on the algebraic Helmholtz inversion (AHI) applied to planar MRE, demonstrating that the deduced phase speed of shear waves depends strongly on the relative orientations of actuator polarization, motion encoding direction and image plane as well as on the actuator plate size, signal-to-noise ratio and discretization of the wave image. Results from the numerical calculation of harmonic elastic waves due to different excitation directions and simulated plate sizes are compared to experiments on a gel phantom. The results suggest that correct phase speed can be obtained despite these largely uncontrollable influences, if AHI is based on out-of-plane displacements and the actuator is driven at an optimal frequency yielding an optimal pixel per wavelength resolution in the wave image. Assuming plane waves, the required number of pixels per wavelength depends only on the degree of noise.

1. Introduction

Magnetic resonance elastography (MRE) is a noninvasive technique used for assessing the elasticity of *in vivo* soft tissues (Muthupillai *et al* 1996, Plewes *et al* 1995). The technique exploits the motion sensitivity of the MR phase signal to detect the propagation of externally induced harmonic shear vibrations inside the human body. MRE is able to measure three-dimensional internal deformation fields which can be used to deduce elastic constants by solving an appropriate inverse problem. Unlike the far more frequently encountered exterior inverse problem relevant in remote sensing, such as radar, sonar (Colton and Kress 1997) and seismology (Aki and Richards 2002), the inverse problem in MRE is to deduce the desired

 © 2008 Institute of Physics and Engineering in Medicine

parameters from interior data. Here, the field is known at the location of the scatterers and in their vicinity. A brief overview of the methods devised for solving the inverse problem in harmonic elastography can be found in the article by Park and Maniatty (2006). Common approaches are made using direct algebraic inversions (Skovoroda *et al* 1995, Sinkus *et al* 2000, Oliphant *et al* 2001, Manduca *et al* 2003), which resemble with certain assumptions and simplifications of the algebraic Helmholtz inversion (AHI). In this study, AHI is investigated for its potential to correctly resolve the phase speed of 3D strain wave fields from scalar wave data acquired within a single image plane. From experimental considerations this planar approach is very useful, since measuring times are shorter and MRI-intrinsic limitations of the image slice thickness are less important than in 3D vector field MRE experiments (Bishop *et al* 2000). For this practical reason, numerous MRE studies on liver and brain have been performed by planar MRE (Rouvière *et al* 2006, Klatt *et al* 2006, Yin *et al* 2007, Sack *et al* 2007, Kruse *et al* 2008). However, the Helmholtz inversion (in both two and three dimensions) requires that the elastic waves are locally well approximated by plane waves. Otherwise, the local wavelengths cannot be related to the underlying elasticities in a straightforward way. Since AHI is based on rather strong assumptions, e.g. no boundary conditions are considered, it is questionable whether these requirements are met. It is expected that the choice of image plane with respect to the direction of actuator motion and motion encoding direction, the size of the actuator plate, the pressure field and boundaries will have an effect on the obtained local wave numbers. This effect can, in principle, be such that one locally has a distribution of wave numbers affected by noise, discreteness of data, diffraction, transducer near field and reflected waves obscuring the meaning of the local wave number, thus rendering its relationship to elasticity very complicated and sensitive to changes in the experimental setup. In the following, these influences are addressed by numerical wave field simulations and planar MRE experiments to derive the limits, in which AHI reproduces reliable phase speed values. The aim of this paper is to develop a setup for the evaluation of planar MRE experiments that helps us to reduce methodological biases, thus increasing the significance of the results.

2. Theory

In the following, we consider an isotropic and linearly elastic infinite medium. The medium is assumed to be homogenous throughout the paper. In the absence of body forces, the equation of motion of the displacement field $\mathbf{u}(\mathbf{r}, t)$ is then given in index notation by

$$\partial_t^2 u_i - c_s^2 \partial_j \partial_j u_i - \left(c_p^2 - c_s^2\right) \partial_j \partial_i u_j = 0, \tag{1}$$

where the index t refers to the derivative with respect to time, while the indices $i, j \in \{1, 2, 3\}$ correspond to the Cartesian coordinates $\{x, y, z\}$. Summation over repeated indices is implied. The parameters c_s and c_p are the phase speeds of the shear and pressure waves, respectively, that are related to the first and second Lamé coefficients μ and λ by

$$c_s = \sqrt{\mu/\rho} \qquad \text{and} \qquad c_p = \sqrt{(\lambda + 2\mu)/\rho}. \tag{2}$$

The inverse problem in MRE is to determine either c_s or c_s and c_p, from the measured displacement field. The density ρ of soft tissue is assumed to be constant. Equation (1) may be separated into two ordinary wave equations (see, e.g., Landau and Lifshitz 1986) by taking note that the total wave field is the sum of the shear field and pressure field $\mathbf{u}(\mathbf{r}, t) = \mathbf{u}^{(s)}(\mathbf{r}, t) + \mathbf{u}^{(p)}(\mathbf{r}, t)$ with

$$\nabla \cdot \mathbf{u}^{(s)} = 0, \tag{3}$$

and

$$\nabla \times \mathbf{u}^{(p)} = \mathbf{0}, \tag{4}$$

i.e. the shear field is volume preserving while the pressure field has no vortices. Under the assumption of harmonic time dependence, which in MRE is enforced by the external vibration source with angular frequency ω and the requirement to establish a steady state, the wave equations become Helmholtz equations for each of the displacement components

$$\triangle u_i^{(s)} + k_s^2 u_i^{(s)} = 0 \qquad \text{with} \quad k_s = \frac{\omega}{c_s}, \tag{5}$$

and

$$\triangle u_i^{(p)} + k_p^2 u_i^{(p)} = 0 \qquad \text{with} \quad k_p = \frac{\omega}{c_p}. \tag{6}$$

Here, $\triangle$ is the Laplacian. Due to their large water content most human soft tissues are almost incompressible (Fung 1993). In incompressible media the majority of elastic energy is carried by the shear wave (Catheline *et al* 1999), which means that $u_i^{(p)}$ is of comparably small amplitude and therefore is often neglected. Then, the only remaining equation is the Helmholtz equation for the shear field (5) in combination with (3), the latter being automatically satisfied by the hypothetical field due to the assumptions.

2.1. The algebraic inversion of the Helmholtz equation in MRE

AHI simply means solving the Helmholtz equation for the wave number. The corresponding indices are omitted in the following, since there is now only a shear field. Thus AHI yields

$$k = \left[-\frac{\triangle u_i(\mathbf{r}, \omega)}{u_i(\mathbf{r}, \omega)} \right]^{1/2}. \tag{7}$$

The wave number carries no index since it is the same for any component $i = x, y, z$ under the assumptions. Moreover, it has been required in writing (7) that the wave is locally a superposition of plane waves featuring the same wave number k and hence k does not depend on the position $\mathbf{r}$ at which (7) is evaluated. Under these conditions we have for the phase speed

$$c = \frac{\omega}{k} \tag{8}$$

and since then

$$c \equiv c_s, \tag{9}$$

the shear elasticity is readily obtained by

$$\mu = \rho c^2. \tag{10}$$

However, under realistic conditions, i.e. in an experiment on gel phantoms, the situation is other than described by the aforementioned equations.

(i) The probed region, e.g. a gel phantom or an organ, is bounded by vessel walls or connective tissue and hence boundary conditions must, in principle, be considered.

(ii) There is a source of waves, i.e. a forced surface traction or a corresponding body force, due to the external actuator. The actuator acts in either shear mode or more often because of efficiency in compressional mode. Depending on its working mode it produces a distinct radiation pattern of elastic waves, and the observed wave field depends on the relative orientations of the actuator polarization $\mathbf{u}_0$, image plane and the motion encoding direction $\mathbf{G}$.

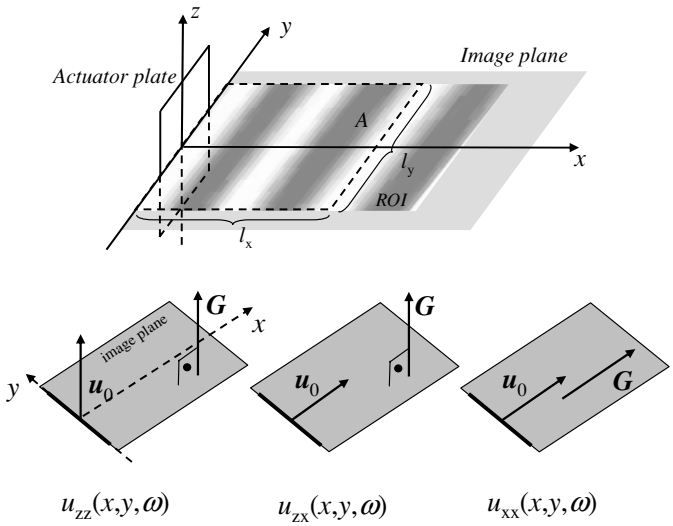

Figure 1. Three configurations of the actuator polarization $\mathbf{u}_0$ and the displacement encoding direction $\mathbf{G}$. The first index in u_{jk} refers to the direction of $\mathbf{G}$ and the second index refers to the direction of $\mathbf{u}_0$. Actuator plate is situated at the head of the image plane (xy) and occupies a region within the yz-plane.

(iii) The elastic waves radiated by a point source acting in an elastic medium are generally non-plane waves and feature a near field with different behavior than the far field. Moreover, the size of the actuator plate determines the observed diffraction.
(iv) The pressure field is not zero.
(v) The measured data are discrete and noisy.

As a result, AHI yields only apparent phase speeds displaying spatial variations also in homogeneous materials:

$$c^* = \frac{\omega}{k^*(x,\, y,\, \omega)}. \tag{11}$$

In the following, c^* is considered as the averaged apparent phase speed in an area $A = l_x l_y$ (see figure 1). Point (i) plays an important role for enforcing the uniqueness of spatially resolved elasticities (Barbone and Gokhale 2004). In the approach made here, boundary effects are diluted by spatial averaging and henceforth neglected. The influences of the points (ii)–(iv) on AHI are investigated by means of a tensor u_{ij} that gives the ith component of the wave field due to an extended actuator vibrating in the j direction. For an arbitrarily oriented actuator the vibration field u_i is a weighted sum of u_{ij} over the index j. In the following section follows a paragraph that accounts for point (v), i.e. biases due to discretization and noise, followed by a section in which the basic equations for calculating u_{ij} in the limit of incompressibility are presented.

2.2. Phase speed dispersion of plane waves due to noise and discretization

Consider an ideal plane wave

$$v(\mathbf{r}) = \mathrm{e}^{\mathrm{i}\mathbf{k}\cdot\mathbf{r}}. \tag{12}$$

Further assume that $\mathbf{k}$ lies within the image plane (xy-plane). The positions at which (12) is known form a discrete square grid with spacing a. Therefore, the position vector $\mathbf{r}$ is uniquely defined by two integer indices m, n and $\mathbf{r} = (x_m, y_n)$ and consequently the plane wave can be labeled $v(\mathbf{r}) = v_{m,n}$. For evaluating the Laplacian in (7) we use a scheme employing repeated central differences. Applied to the plane wave (12) the scheme yields the approximation

$$\hat{D}v_{m,n} = \frac{1}{4a^2}(v_{m+2,n} - 2v_{m,n} + v_{m-2,n} + v_{m,n+2} - 2v_{m,n} + v_{m,n-2}), \tag{13}$$

where $\hat{D}$ is the finite difference approximation to the Laplace operator. Let the wave vector be $\mathbf{k} = (k, 0)$, where $k = \omega/c$. Then AHI together with the approximation scheme (13) applied to (12) yields for the apparent phase speed

$$c_0^* = \frac{a\omega\sqrt{2}}{\sqrt{1 - \cos 2ka}}. \tag{14}$$

For including noise, the wave (12) must be replaced by

$$v'_{m,n} = v_{m,n} + \sigma w_{m,n}, \tag{15}$$

where $w_{m,n}$ assumes random values, that are normally distributed with zero mean and σ is the noise-to-signal ratio. The apparent wave number then reads

$$\begin{aligned} k^* &= \left(-\frac{\hat{D}v_{m,n}}{v_{m,n} + \sigma w_{m,n}} - \frac{\sigma \hat{D}w_{m,n}}{v_{m,n} + \sigma w_{m,n}} \right)^{1/2} \\ &= \left(-\frac{\hat{D}v_{m,n}}{v_{m,n}} \frac{1}{1 + \sigma w_{mn}/v_{mn}} - \frac{\hat{D}w_{m,n}}{w_{m,n}} \frac{\sigma}{v_{mn}/w_{mn} + \sigma} \right)^{1/2} \\ &= \left(\frac{k_0^2}{1 + \sigma^2} + \frac{k_{\text{noise}}^2}{1/\sigma^2 + 1} \right)^{1/2} \\ &\approx \left(\frac{k_0^2}{1 + \sigma^2} + \frac{1}{a^2} \frac{1}{1/\sigma^2 + 1} \right)^{1/2}, \end{aligned} \tag{16}$$

where $k_0 = \omega/c_0^*$ and the approximation $w_{mn}/v_{mn} \approx \sigma$ is used. The wave number $k_{\text{noise}} \approx 1/a$ was found empirically through the application of AHI to pure random noise. Expanding $c^* = \omega/k^*$ to first order in σ^2, one obtains for the apparent phase speed

$$c^* \approx \frac{\omega}{k_0} \left[1 - \frac{\sigma^2}{2} \left(\frac{1}{a^2 k_0^2} - 1 \right) \right]. \tag{17}$$

Expression (17) gives the dispersion of the apparent phase speed for the plane wave model at low σ. Equating $k = k^*$ (16), using (14) and substituting $\Omega = ka$ yields the equation

$$\Omega = \left(\frac{1 - \cos 2\Omega}{2} \frac{1}{1 + \sigma^2} + \frac{1}{1/\sigma^2 + 1} \right)^{1/2} \tag{18}$$

for which, to the best of our knowledge, there is no solution known in closed form. Noting that $\lambda/a = 2\pi/\Omega$, equation (18) enables the numerical calculation of the number of pixels per wavelength required for AHI to yield the correct phase speed, i.e. $c^* = c$, depending only on the noise level.

2.3. Shear wave field in an incompressible quasi-half space due to an extended source

Assuming a square actuator plate of size d that is located in the xy-plane and is acting into the j-direction (see also figure 1), the kth component of the shear wave field can be written as

$$u_{jk}(\mathbf{r}, \omega) = \int_{-d/2}^{d/2} \int_{-d/2}^{d/2} \bar{h}_{jk}(\mathbf{r} - \mathbf{R}, \omega)\, \mathrm{d}Y\, \mathrm{d}Z. \tag{19}$$

Here, $\bar{h}_{jk}$ represents an appropriate expression for the field produced by a point source on the surface of an isotropic half-space. Here we use a quasi-half-space model first suggested by Lhémery (1994) and extended by Sandrin *et al* (2004) by including the near-field term. However, we only take those parts into account that remain in the limit of incompressibility, i.e. as c_s/c_p approaches zero. Moreover, the field is multiplied by the Fourier transform of a sinusoidal source time function to model the field due to a harmonic source. It reads

$$\begin{aligned}\bar{h}_{jk}(\mathbf{r}, \omega) = &-\frac{\mathrm{i}}{2\rho c^2}(\gamma_j\gamma_k - \delta_{jk})\frac{1}{r}\,\mathrm{e}^{\mathrm{i}\omega r/c} \\ &+ \frac{\mathrm{i}}{2\rho\omega^2}(3\gamma_j\gamma_k - \delta_{jk})\frac{1}{r^3}\left[\left(1 - \frac{\mathrm{i}\omega r}{c}\right)\mathrm{e}^{\mathrm{i}\omega r/c} - 1\right],\end{aligned} \tag{20}$$

where $\gamma_j = x_j/r$ and δ_{ij} is the Kronecker delta. The first term in (20) is the shear far field. The second term comprises two parts of which the oscillatory part represents the shear near field and the nonoscillatory part is the remainder of the pressure field in the limit of incompressibility. Since there is no analytic solution available to (19), it is treated numerically.

3. Methods

To experimentally prove the influence of discretization and noise on AHI, a plane-wave MRE experiment was performed on a gel phantom made of 1 : 5 parts of Wirogel (Bego Inc., Bremen, Germany) : water. MRI scanner, coil and actuator setup were identical to experiments described in Papazoglou *et al* (2007). A square-plate actuator of $d = 8.5$ cm edge size attached to the top surface of the phantom was vibrated with a variable driving frequency from $f = 10$ to 100 Hz for changing the spatial resolution of the waves given in wavelengths per pixel size (λ/a) with $a = 1.5$ mm. The orientation of the image slice, the vibration direction and the direction of motion sensitization were adjusted for the acquisition of $u_{zz}(x, y, \omega)$ wave images according to figure 1. For data processing, wave images were low-pass filtered using a Butterworth filter ($k_0 = 1000\ \mathrm{m}^{-1}$) and inverted using the Matlab function (The MathWorks Inc., Natick, MA, USA) given in the appendix. c^* was derived as a mean quantity from a ROI with $l_x = 10.6$ cm and $l_y = 8.5$ cm edge size (see figure 1). An edge of two pixels was eroded from the outer boundaries of the ROI in order to mitigate uncertainties of the used finite difference scheme (13) due to unknown boundary conditions. The surface integral (19) was numerically evaluated using the adaptive Simpson quadrature of Matlab at different plate sizes from $d = 1.5$ to 100 mm, driving frequencies from $f = 10$ to 100 Hz and the three configurations shown in figure 1. A phase speed of $c = 0.81\ \mathrm{m\ s}^{-1}$ was used in the simulations similar to the experimental value which was deduced by a 1D fit of wave profiles. To model noise, separate sets of normally distributed random numbers with variance sigma and zero mean were added to the real and imaginary parts of the simulated

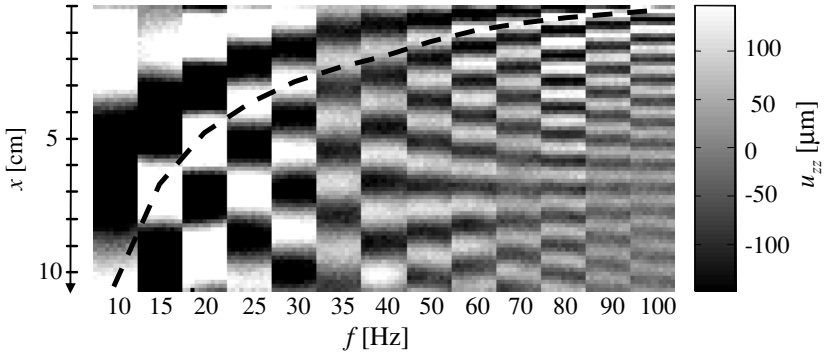

Figure 2. Sections of out-of-image plane wave images obtained from an experiment on a gel phantom. The configuration corresponds to simulations of $u_{zz}(x, y, \omega)$ (see figure 1). Waves are coupled into the gel phantom by an actuator plate located on top, hence the propagation direction is from top to bottom. The dashed line corresponds to the wavelength obtained from $\lambda = c/f$.

displacement fields. Equation (18) was numerically solved for sigma using Maple (Maplesoft, Waterloo, ON, Canada).

4. Results

Manual evaluation of 1D profiles in the direction of the experimental wave propagation (figure 2) yielded a phase speed of $c = 0.81 \pm 0.02$ m s^{-1}. This phase speed was used as a gold standard for further analysis. The corresponding wavelengths $\lambda = c/f$ in the frequency range between 10 and 100 Hz are plotted onto the wave images. This demonstrates the absence of intrinsic wave dispersion as the λ-graph approximately crosses each wave-image section at a one wavelength distance from the actuator. The situation changes if c is determined by inversion using (7) with the discrete Laplacian (13). Figure 3 shows the dispersion of the apparent phase speed c^* over λ/a that is proportional to $1/f$. The overshot of c^* at low λ/a values, i.e. at high driving frequencies, is due to discretization, whereas the underestimation of c^* at low driving frequencies is the result of noise. At a resolution of $\lambda/a \approx 24$ the apparent phase speed coincides with the true speed, which is in excellent agreement with approximation (17). To further investigate at which optimal resolution an MRE experiment should be run, numerical solutions of equation (18) are plotted in figure 4 and compared with AHI applied to simulated and experimental plane waves. There, the theory tends to overestimate the optimal λ/a, whereby the observed deviation causes a λ/a error of approximately 5%. Figure 5 shows the results for AHI applied to simulated wave fields produced by actuator plates of various sizes. In the absence of noise, AHI based on the out-of-plane displacement $u_{zz}(x, y, \omega)$ or $u_{zx}(x, y, \omega)$ is less biased by diffraction than the AHI based on $u_{xx}(x, y, \omega)$. In particular, at the plate size used in the experiment, $u_{xx}(x, y, \omega)$ yields strongly overestimated values c^*. However, also out-of-plane displacement modes are influenced by the extension of the driver. A threshold appears when the actuator plate exceeds one wavelength ($d \approx \lambda$), causing c^* to increase by about 10% due to diffraction. For $d > 2\lambda$ variation is only shallow for $u_{zz}(x, y, \omega)$ and $u_{zx}(x, y, \omega)$. The deviation from $c = 0.81$ m s^{-1} of all wave modes at $d = 0$ is due to discretization similarly to the data at low λ/a seen in figure 3. Figure 6(a) shows that the half-space model used predicts an overestimation of c within the entire parameter range if data are noiseless. This effect is the result of wave diffraction due to an extended source. However,

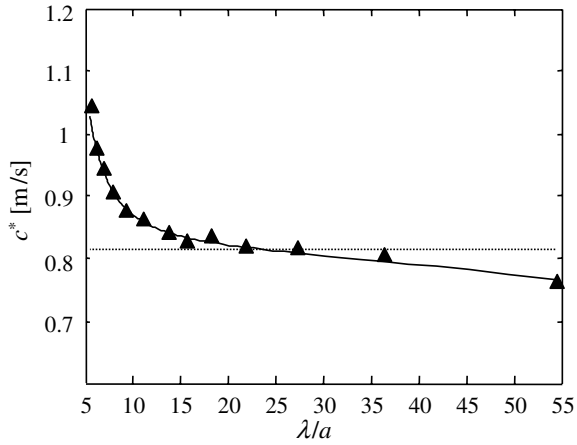

Figure 3. Apparent phase speed as a function of pixel per wavelength obtained by applying AHI to waves measured in gel and averaging over a ROI as given in the methods section (triangles). Phase speed according to (14) (straight line). $c^\star$ according to (17) with $\sigma = 0.03$ (dashed line). Phase speed obtained from the one-dimensional fit of profiles applied to wave images in figure 2 (dotted line).

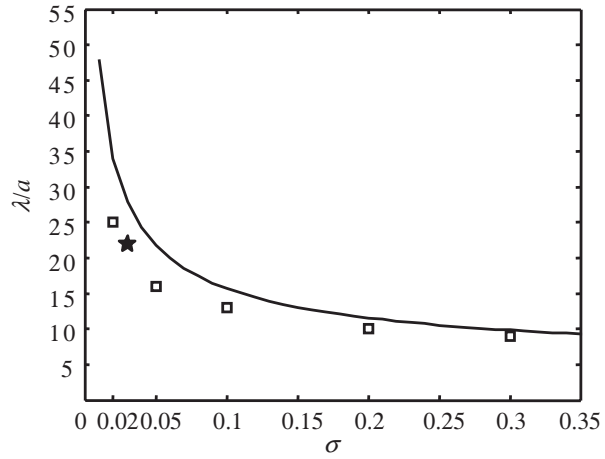

Figure 4. Number of pixels required for AHI to yield the correct phase speed as found from the numerical solution of equation (18) (straight line), AHI applied to simulated plane waves with noise (squares) and AHI applied to wave images measured in a phantom experiment (star) (point of intersection in figure 3).

if noise is added c^* decreases below 0.81 m s^{-1} for $\lambda/a > 20$ as shown in figure 6(b). The out-of-plane displacement modes u_{zz} and u_{zx} resemble the behavior of c^* observed in the experiment and in the plane wave model of figure 3. In contrast, the in-plane polarization u_{xx} causes a strong deviation of c^* from the plane-wave behavior, although these waves have their optimum resolution at $\lambda/a = 21$, which is similar to c^* deduced from u_{zz}. However, the steep slope of c^* of u_{xx} near the intersection with c results in greater inaccuracies of c^* than expected for u_{zx}, whose shallow slope allows λ/a to be varied between 15 and 30 without exceeding an error of c^* of 5%.

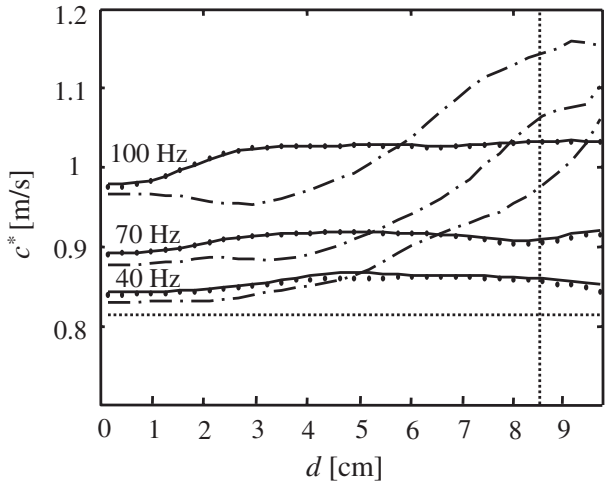

Figure 5. Apparent phase speed obtained from AHI applied to simulated waves according to (19) as a function of the plate size d for the three configurations shown in figure 1. Inversion based on $u_{zz}(x, y, \omega)$ (straight line), inversion based on $u_{zx}(x, y, \omega)$ (dots) and inversion based on $u_{xx}(x, y, \omega)$ (dash-dotted line). The straight dotted horizontal line shows the true phase speed $c = 0.81$ m s^{-1} used in the simulations, while the vertical line corresponds to the plate size $d = 8.5$ cm used in the experiment.

5. Discussion and conclusion

Our results demonstrate that AHI based on discrete and noisy wave data yields frequency-dependent apparent phase speeds (figure 3), even when the material is not intrinsically dispersive. The good accordance of the plane-wave model (17) with experimental and simulated data shown in figures 3 and 4 suggest that at low λ/a second derivatives in (13) yield an overestimated apparent phase speed, while at large λ/a noise acts to decrease the speed below the true value. Between these two cases an optimal λ/a exists, where the true phase speed is observed. However, biases due to diffraction cannot be entirely excluded. Simulations with extended plate sizes were conducted to tackle this question. The results in figures 5 and 6 show that diffraction biases on c^* can be minimized by using out-of-plane image data for AHI. There, the pressure field is less present than in the case of $u_{xx}(x, y, \omega)$, as given in (20). We conclude from this that the presence of a pressure field in this direction is responsible for the strongly varying apparent phase speed obtained from in-plane data. Moreover, the ROI encloses only one to two wavelengths at large λ/a or correspondingly at low driving frequencies. In contrast to the simple plane-wave model, the half-space model features a near field in this region, which shows different wave numbers than the far field as seen from the rise in c^* with increasing λ/a in figure 6(a). If the plate size is large and the frequencies are low along with a ROI close to the actuator plate, this leads to overestimated phase speeds in agreement with the findings by Sandrin *et al* (2004), whereby $u_{zz}(x, y, \omega)$ is least affected. Finally, the situation close to the source could be further complicated by surface effects such as head waves (Benech and Negreira 2005) or Rayleigh waves (Aki and Richards 2002), which are not included in our model. Therefore, our recipe for minimizing systematic errors in the apparent phase speed is as follows: AHI should be based on out-of-plane displacement, with a direction of motion encoding that is preferably parallel to the direction of actuator motion. The

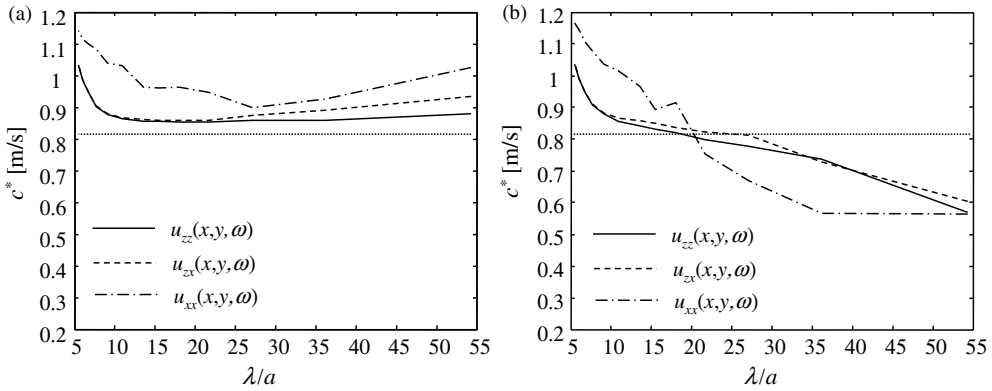

Figure 6. c^* as a function of λ/a for three configurations in figure 1 at plate size $d = 8.5$ cm corresponding to the experiment. (a) (No noise added) straight line: inversion based on $u_{zz}(x, y, \omega)$, dashed line: inversion based on $u_{zx}(x, y, \omega)$ and dash-dotted line: inversion based on $u_{xx}(x, y, \omega)$. (b) The same as (a) with $\sigma = 0.1$. Dotted line: phase speed used in the simulations.

phase speed should be spatially averaged in order to better approach a plane-wave behavior of experimental waves and thus to minimize biases on c^* due to diffraction and near field. Then, the dispersion is mainly governed by noise and discretization in accordance with (17) and allows the deduction of correct phase speed, if the optimal λ/a at the given noise-to-signal ratio is chosen. Instead of consulting figure 4 to find the optimal λ/a, the fitting function $\lambda/a \approx 2\sqrt{2}\pi/\sigma$ can be used to directly calculate the required resolution. Though this paper demonstrates the potential of AHI to deduce correct phase speeds and thus shear moduli from planar MRE data, further investigation is required to elaborate the size and the position of the ROI relative to the actuator geometry in order to achieve a wave behavior that is, in its mean, satisfyingly close to plane waves. Furthermore, it should be noted that filters, like those for suppressing noise, change the effective wavelengths in the image. Thus, a careful match of filter threshold (Klatt *et al* 2007) may be able to compensate for dispersive effects as seen in figure 3. However, this does not impair principal findings of this study, since the refinement of filter parameters is surely improved by knowing about the demonstrated AHI-intrinsic biases. Finally, although this study was strictly carried out for two dimensions, similar effects of noise and discretization as discussed here are expected for 3D inversion techniques. One important source of error in planar MRE is not relevant in 3D methods: the occurrence of geometrical biases as investigated by Hamhaber *et al* (2007) and Klatt *et al* (2006) for MRE on brain and liver. As this effect is not specifically related to AHI, it has not been analyzed here, although it should be added to the list of requirements in planar MRE experiments.

In summary, we have investigated the effects of discretization, noise and diffraction on average phase speeds obtained from AHI applied to scalar MRE wave data. A simple model was developed for plane waves that yields dispersion in the apparent phase speed due to noise and discretization, which is in very good agreement to simulations and experiment on a phantom. It was demonstrated that AHI is capable of reconstructing correct phase speed data (and therefore correct elasticities) from planar MRE wave images if this inversion-intrinsic dispersion is taken into account.

Appendix

AHI code for Matlab

```
function cstar = ahi(data, freq, pixsize)

% Build k-space
origin = floor(size(data)./2)+1;
[kx, ky] = meshgrid(1-origin(2):1:size(data, 2)-origin(2),...
    1-origin(1):1:size(data, 1)-origin(1));
kx = 2*pi/size(data, 2)/pixsize(2)*kx;
ky = 2*pi/size(data, 1)/pixsize(1)*ky;

% Replace zeros in data
data(data==0) = eps;

% Filter data
filter = 1./(1+(sqrt(kx.^2+ky.^2)/1000).^(4));
ft = fftshift(fft2(data));
data = ifft2(ifftshift(filter.*ft));

% Compute second derivatives
[ux, uy] = gradient(data, pixsize(1), pixsize(2));
[uxx, uyx] = gradient(ux, pixsize(1), pixsize(2));
[uxy, uyy] = gradient(uy, pixsize(1), pixsize(2));

% Helmholtz inversion and averaging
tmp = 2*pi*freq./real(sqrt((uxx+uyy)./(-(data))));
tmp = tmp(3:end-2, 3:end-2);
cstar = median(tmp(:));
```

References

Aki K and Richards P G 2002 *Quantitative Seismology* (Sausalito: University Science Books)

Barbone P E and Gokhale N H 2004 Elastic modulus imaging: on the uniqueness and nonuniqueness of the elastography inverse problem in two dimensions *Phys. Med. Biol.* **20** 283–96

Benech N and Negreira C A 2005 Longitudinal and lateral low frequency head wave analysis in soft media *J. Acoust. Soc.* **117** 3424–30

Bishop J, Samani A, Sciaretta J and Plewes D B 2000 Two-dimensional MR elastography with linear reconstruction: methodology and noise analysis *Phys. Med. Biol.* **45** 2081–91

Catheline S, Francois W and Fink M 1999 A solution to diffraction biases in sonoelasticity: the acoustic impulse technique *J. Acoust. Soc.* **105** 2941–50

Colton D L and Kress R 1997 *Inverse Acoustic and Electromagnetic Scattering Theory* (*Applied Mathematical Sciences*) (Berlin: Springer)

Fung Y C 1993 *Biomechanics* (New York: Springer)

Hamhaber U, Sack I, Papazoglou S, Rump J, Klatt D and Braun J 2007 Three-dimensional analysis of shear wave propagation observed by *in vivo* magnetic resonance elastography of the brain *Acta Biomater.* **3** 127–37

Klatt D, Asbach P, Rump J, Papazoglou S, Somasundaram R, Modrow J, Braun J and Sack I 2006 *In vivo* determination of hepatic stiffness using steady-state free precession magnetic resonance elastography *Invest. Radiol.* **41** 841–8

Klatt D, Hamhaber U, Asbach P, Braun J and Sack I 2007 Noninvasive assessment of the rheological behavior of human organs using multifrequency MR elastography: a study of brain and liver viscoelasticity *Phys. Med. Biol.* **52** 7281–94

Kruse S A, Rose G H, Glaser K J, Manduca A, Felmlee J P, Jack C R Jr and Ehman R L 2008 Magnetic resonance elastography of the brain *Neuroimage* **39** 231–7

Landau L D and Lifshitz E M 1986 *Theory of Elasticity* (Oxford: Butterworth-Heinemann)

Lhémery A 1994 A model for the transient ultrasonic field radiated by an arbitrary loading in a solid *J. Acoust. Soc.* **96** 3776–86

Manduca A, Lake D S, Kruse S A and Ehman R L 2003 Spatio-temporal directional filtering for improved inversion of MR elastography images *Med. Image Anal.* **7** 465–73

Muthupillai R, Rossman P J, Lomas D J, Greenleaf J F, Riederer S J and Ehman R L 1996 Magnetic resonance imaging of transverse acoustic strain waves *Magn. Reson. Med.* **36** 266–74

Oliphant T E, Manduca A, Ehman R L and Greenleaf J F 2001 Complex-valued stiffness reconstruction for magnetic resonance elastography by algebraic inversion of the differential equation *Magn. Reson. Med.* **45** 299–310

Papazoglou S, Hamhaber U, Braun J and Sack I 2007 Horizontal shear wave scattering from a nonwelded interface observed by magnetic resonance elastography *Phys. Med. Biol.* **52** 675–84

Park E and Maniatty A M 2006 Shear modulus reconstruction in dynamic elastography: time harmonic case *Phys. Med. Biol.* **51** 3697–721

Plewes D B, Betty I, Urchuk S N and Souter I 1995 Visualizing tissue compliance with MR imaging *J. Magn. Reson. Imaging* **5** 733–8

Rouvière O, Yin M, Dresner M A, Rossman P J, Burgart L J, Fidler J L and Ehman R L 2006 MR elastography of the liver: preliminary results *Radiology* **240** 440–8

Sack I, Beierbach B, Hamhaber U, Klatt D and Braun J 2007 Non-invasive measurement of brain viscoelasticity using magnetic resonance elastography *NMR Biomed.* DOI: 10.1002/nbm.1189

Sandrin L, Cassereau D and Fink M 2004 The role of the coupling term in transient elastography *J. Acoust. Soc.* **115** 73–83

Sinkus R, Lorenzen J, Schrader D, Lorenzen M, Dargatz M and Holz D 2000 High-resolution tensor MR elastography for breast tumor detection *Phys. Med. Biol.* **45** 1649–64

Skovoroda A, Emilianov S and O'Donnel M 1995 Tissue elasticity reconstruction based on ultrasonic displacement and strain images *IEEE Trans. Ultrason. Ferroelectr. Freq. Control* **42** 747–65

Yin M, Talwalkar J A, Glaser K J, Manduca A, Grimm R C, Rossman P J, Fidler J L and Ehman R L 2007 Assessment of hepatic fibrosis with magnetic resonance elastography *Clin. Gastroenterol. Hepatol.* **5** 1144–6